







Enhanced magnetization of the highest- T_C ferrimagnetic oxide $\text{Sr}_2\text{CrOsO}_6$

Jie Chen ^{1,2,*}, Xiao Wang,³ Zhiwei Hu,³ Liu Hao Tjeng ³, Stefano Agrestini,⁴ Manuel Valvidares ⁴, Kai Chen ⁵, Lucie Nataf,⁶ Francois Baudelet,⁶ Masahiro Nagao,⁷ Yoshiyuki Inaguma,⁸ Alexei A. Belik ¹, Yoshihiro Tsujimoto,^{1,2} Yoshitaka Matsushita ⁹, Taras Kolodiaznyi,¹ Raimundas Sereika,¹⁰ Masahiko Tanaka,¹¹ and Kazunari Yamaura^{1,2}

¹International Center for Materials Nanoarchitectonics (WPI-MANA), National Institute for Materials Science, 1-1 Namiki, Tsukuba, Ibaraki 305-0044, Japan

²Graduate School of Chemical Sciences and Engineering, Hokkaido University, North 10 West 8, Kita-ku, Sapporo, Hokkaido 060-0810, Japan

³Max Planck Institute for Chemical Physics of Solids, Nöthnitzer Strasse 40, 01187 Dresden, Germany

⁴ALBA Synchrotron Light Source, E-08290 Cerdanyola del Vallès, Barcelona, Spain

⁵Helmholtz-Zentrum Berlin für Materialien und Energie, Albert-Einstein-Straße 15, 12489 Berlin, Germany

⁶Synchrotron SOLEIL, L'Orme des Merisiers, Saint-Aubin, 91192 Gif-sur-Yvette Cedex, France

⁷Institute of Materials and Systems for Sustainability, Nagoya University, Nagoya 464-8601, Japan

⁸Department of Chemistry, Faculty of Science, Gakushuin University, 1-5-1 Toshima-ku, Tokyo 171-8588, Japan

⁹Materials Analysis Station, National Institute for Materials Science, 1-2-1 Sengen, Tsukuba, Ibaraki 305-0047, Japan

¹⁰Vytautas Magnus University, K. Donelaičio 58, Kaunas 44248, Lithuania

¹¹Synchrotron X-ray Station at SPring-8, National Institute for Materials Science, Kouto 1-1-1, Sayo-cho, Hyogo 679-5148, Japan



(Received 9 August 2020; accepted 23 October 2020; published 16 November 2020)

The double perovskite oxide $\text{Sr}_2\text{CrOsO}_6$ with a $3d^3$ - $5d^3$ configuration exhibits very high- T_C ferrimagnetism (~ 725 K) at the end point of half-metallicity. Many substitution studies have been conducted theoretically and experimentally over the last two decades to shed more light on the open issue of how the $3d^3$ - $5d^3$ configuration generates the high- T_C ferrimagnetic state and to accelerate development toward applications. We have succeeded in synthesizing a solid solution of $\text{Sr}_2\text{Cr}_{1-x}\text{Ni}_x\text{OsO}_6$ under high-pressure and high-temperature conditions. $\text{Sr}_2\text{Cr}_{0.5}\text{Ni}_{0.5}\text{OsO}_6$ exhibits magnetization sixfold greater ($\sim 1.2 \mu_B$ /formula unit at 5 K) than that of $\text{Sr}_2\text{CrOsO}_6$. This enhancement is preserved even at room temperature. X-ray absorption spectroscopy revealed that the electronic configuration is $\text{Sr}_2(\text{Cr}^{3+}_{2/3}\text{Cr}^{6+}_{1/3})_{0.5}\text{Ni}^{2+}_{0.5}\text{Os}^{5+}\text{O}_6$, indicating that the valence state of Os does not change from the host state $[\text{Os}^{5+}(5d^3)]$. Instead, nonmagnetic $\text{Cr}^{6+}(3d^0)$ is partly generated among coexisting $\text{Cr}^{3+}(3d^3)$. X-ray magnetic circular dichroism measurements showed that the Os ions are antiferromagnetically coupled to the Cr and ferromagnetically to the Ni. The replacement of antiferromagnetic Cr by ferromagnetic Ni explains the increase of the net magnetism in this ferrimagnetic system. We infer that the strong antiferromagnetic exchange interaction of the $3d^3$ - $5d^3$ configuration associated with the Cr^{3+} -O- Os^{5+} bond still accounts for the robust high- T_C ferrimagnetism of the Ni-substituted series. We deduce from the experiments that the ferromagnetic exchange interaction of the $3d^8$ - $5d^3$ configuration of the Ni^{2+} -O- Os^{5+} is stronger than that of the $3d^8$ - $3d^3$ configuration of the Ni^{2+} -O- Cr^{3+} , suggesting that the larger $5d$ orbital of the Os allows for a stronger virtual hopping from the Ni than the smaller $3d$ orbital of the Cr. The present results can help to further develop practical materials and to resolve open issues concerning the relative strengths of the various exchange interactions.

DOI: [10.1103/PhysRevB.102.184418](https://doi.org/10.1103/PhysRevB.102.184418)

I. INTRODUCTION

Half-metallic materials with a high Curie temperature (T_C) have attracted considerable attention over several decades because of their promising properties for applications using spintronics. A high T_C improves the feasibility of new devices that operate at room temperature. Half-metallic $\text{Sr}_2\text{FeMoO}_6$

with a T_C of 420 K was discovered in the double perovskite oxide material category in 1998 [1]. This was followed by sequential synthesis of analogous half-metals and ferrimagnets such as $\text{Sr}_2\text{CrReO}_6$ (635 K [2,3]), $\text{Sr}_2\text{CrMoO}_6$ (450 K [4]), $\text{Sr}_2\text{FeReO}_6$ (400 K [5]), and Sr_2CrWO_6 (390 K [6]). Similar Ca and Ba families were synthesized, but their T_C s were usually lower than those of the Sr family [7].

The general formula of the half-metallic and ferrimagnetic (FIM) double perovskite oxide is $\text{Sr}_2\text{BB}'\text{O}_6$, where B and B' , respectively, are $3d$ and $4d/5d$ transition metals. Among this family, $\text{Sr}_2\text{CrOsO}_6$ ($3d^3$ - $5d^3$) is notable because of its electronic state, in which the majority-spin orbital is empty

*Corresponding author: International Center for Materials Nanoarchitectonics (WPI-MANA), National Institute for Materials Science, 1-1 Namiki, Tsukuba, Ibaraki 305-0044, Japan; is.jiechen@gmail.com

and the minority-spin orbital is fully occupied. This state is primarily activated by $\text{Cr}^{3+}(3d^3, t_{2g}^3)$ and $\text{Os}^{5+}(5d^3, t_{2g}^3)$, and can be regarded as the end point of half-metallicity [8]. Although slightly different T_C s such as 725 K [8] and 660 K [9] have been independently reported, probably because of the different degrees of antisite disorder, its T_C is the highest among all bulk oxides.

Theoretically Lee and Pickett proposed that $\text{Sr}_2\text{CrOsO}_6$ is a near-half-metallic antiferromagnet with a large spin-orbit coupling (SOC), which significantly reduces the Os magnetic moment [10]. In an independent study, a multiorbital model was used to characterize the electronic state of $\text{Sr}_2\text{CrOsO}_6$, implying that $\text{Sr}_2\text{CrOsO}_6$ is a Mott insulator rather than a SOC-driven insulator [11]. Meanwhile, it was claimed that the high- T_C FIM state can be understood within a kinetic energy driven exchange scheme [8,12,13]. Regardless of the driving mechanism, the high- T_C FIM properties are useful and, thus, the improvement of the electronic and magnetic properties of $\text{Sr}_2\text{CrOsO}_6$ has been of significant interest.

It is claimed that the high T_C is associated with the bandwidth of the minority-spin channel [8,14]. Based on this scheme, La^{3+} was substituted for Sr^{2+} . In testing, a T_C increase of more than 100 K was attained by LaSrFeMoO_6 and LaCaCrWO_6 [15,16]. Likewise, a partial substitution of the 5d transition metal is expected to further increase the T_C [3,6]. Besides, the hypothetical compound “ $\text{Sr}_2\text{CrIrO}_6$ ” has been suggested to possess a much higher T_C than that of $\text{Sr}_2\text{CrOsO}_6$ [7,17].

The effect of replacing Cr by other 3d elements, especially by a divalent 3d metal ion, on the physical properties of $\text{Sr}_2\text{CrOsO}_6$ has not been researched thoroughly. In this study, the substitution of Ni for Cr in $\text{Sr}_2\text{CrOsO}_6$ was achieved when a series of polycrystalline $\text{Sr}_2\text{Cr}_{1-x}\text{Ni}_x\text{OsO}_6$ ($x = 0, 0.25, 0.5$, and 1) was successfully prepared under high-pressure and high-temperature conditions. The substitution changed the lattice symmetry, and the electronic and magnetic properties. Surprisingly, the half substituted $\text{Sr}_2\text{Cr}_{0.5}\text{Ni}_{0.5}\text{OsO}_6$ exhibits magnetization sixfold greater [$\sim 1.2 \mu_B/\text{formula unit (f.u.)}$ at 5 K] than that of $\text{Sr}_2\text{CrOsO}_6$. This enhancement is preserved even at room temperature; these features were not expected in the schemes to date.

II. EXPERIMENT

Polycrystalline $\text{Sr}_2\text{Cr}_{1-x}\text{Ni}_x\text{OsO}_6$ ($x = 0, 0.25, 0.5, 1$) was synthesized by a solid-state reaction in a highly compressed capsule from the powders of SrO (99.9%, Strem Chemicals, Inc.), CrO_2 (Magtrieve, Sigma-Aldrich Co.), NiO (99.97%, High Purity Chemicals Co., Ltd.), OsO_2 (lab-made from Os powder, 99.95%, supplied by Nanjing Dongrui Platinum Co., Ltd.), and KClO_4 (>99.5%, Kishida Chemical Lab. Co., Ltd.). The powders were thoroughly mixed in a stoichiometric ratio, followed by being sealed in a Pt capsule. The preparation was conducted in an Ar-filled glove box. Under 6 GPa pressure generated by a belt-type pressure apparatus (Kobe Steel, Ltd.), the capsule was heated to a target temperature and held there for 60 min. For the $\text{Sr}_2\text{Cr}_{1-x}\text{Ni}_x\text{OsO}_6$ ($x = 0, 0.25, 0.5$) the temperature was 1600 °C, and for the $\text{Sr}_2\text{NiOsO}_6$ it was 1300 °C. After heating, the capsule was quenched to 100 °C

or below within 1 min, following which the pressure was gradually released.

The quality of the high-pressure synthesized products was investigated by powder x-ray diffraction (XRD) using Cu $K\alpha$ radiation in a commercial apparatus (MiniFlex 600, Rigaku Co, Ltd). In addition, structural refinement was carried out at 750, 550, and 454 K, and room temperature by synchrotron XRD using a high-precision powder x-ray diffractometer installed at the BL15XU beamline, SPring-8 [18,19]. A Rietveld analysis using RIETAN-FP and VESTA software [20,21] was applied to the synchrotron XRD patterns.

The magnetic properties were measured at temperatures between 2 and 400 K in a magnetic property measurement system (MPMS, Quantum Design, Inc.). The magnetic susceptibility (χ) was measured in a magnetic field (H) of 10 kOe under field-cooling (FC) and zero-field-cooling (ZFC) conditions. The isothermal magnetization (M) was measured in a field range between -70 and $+70$ kOe at 5 K. The high-temperature χ was measured from 300 to 950 K using a vibrating sample magnetometer (VSM, Riken Denshi Co, Ltd.) in a 10-kOe magnetic field. The copper sample container’s contribution was subtracted from the raw data. The VSM data were calibrated by the room-temperature χ measured in the MPMS using the same powder.

The electrical transport and specific heat capacity (C_p) were measured using a physical property measurement system (PPMS, Quantum Design, Inc.). Silver paste and platinum wires connected the plateletlike piece to the device terminals for transport measurement. The C_p was measured by a thermal-relaxation method at temperatures from 300 to 2 K using Apiezon-N grease for thermal contact between the polycrystal and the sample stage. The Raman spectra were measured on a Renishaw inVia spectrometer with a 532-nm-laser wavelength. The laser power was 5.8 mW and a data-collection period of 120 s was maintained for each spectrum. Heating from 295 to 470 K was carried out in a normal air atmosphere. For the dielectric and complex impedance studies, silver ink electrodes were applied and dried in a glove box. The dielectric properties were measured using an Alpha impedance analyzer (Novocontrol Technologies GmbH & Co. KG) in the temperature range of 2– 00 K.

X-ray absorption spectroscopy (XAS) and x-ray magnetic circular dichroism (XMCD) experiments at the Cr- $L_{2,3}$ and Ni- $L_{2,3}$ absorption edges were performed at the BL29 BOREAS beamline in the ALBA synchrotron radiation facility [22]. Circularly polarized light was used with the photon either spin parallel (μ^+) or antiparallel (μ^-) to the magnetic field. The degree of circular polarization at the Cr- $L_{2,3}$ and Ni- $L_{2,3}$ edges was close to 100%. The spectra were recorded using a total electron yield method by measuring the sample drain current in a vacuum chamber at a pressure of 2×10^{-10} mbar. The XAS measurements for Cr, Ni, and Os were conducted at 300 K. The XMCD at the Cr- $L_{2,3}$ and Ni- $L_{2,3}$ edges was collected at a temperature of 25 K in a 60-kOe field. The XMCD at the Os- $L_{2,3}$ edges was performed at the ODE beamline of the Synchrotron Soleil in the transmission mode at 10 K with a 13-kOe field. We obtained the numerical spin and orbit moments by the sum-rule calculation as proposed by

Thole and Carra *et al.* [23,24];

$$m_{\text{orb}} = -\frac{4 \int_{L_3+L_2} (\mu^+ - \mu^-) dE}{3 \int_{L_3+L_2} (\mu^+ + \mu^-) dE} (10 - n_d),$$

$$m_{\text{spin}} + 7 \langle T_z \rangle = -\frac{6 \int_{L_3} (\mu^+ - \mu^-) dE - 4 \int_{L_3+L_2} (\mu^+ - \mu^-) dE}{\int_{L_3+L_2} (\mu^+ + \mu^-) dE} (10 - n_d),$$

where n_d is the electrons occupying the d orbitals in a transition metal, μ^+ (μ^-) is the XAS spectrum with the magnetic field parallel (antiparallel) to the spin of the incident light, and the subscripts L_3 and L_2 indicate the integrated region. The term $\langle T_z \rangle$ is the intra-atomic dipole moment and is very small for transition metal ions in octahedral coordination [25,26].

$\text{Sr}_2\text{Cr}_{0.5}\text{Ni}_{0.5}\text{OsO}_6$ with a T_C of 454 K was selected for further investigation using a transmission electron microscope (JEM2010, JEOL Ltd.) equipped with a heating stage. The accelerating voltage was 200 kV. The compound was heated beyond T_C and then cooled to room temperature; the heating cycle was repeated several times and observation by electron diffraction was conducted occasionally. The patterns were recorded on imaging plates.

III. RESULTS AND DISCUSSION

A. Crystal structure

The powder XRD patterns for $\text{Sr}_2\text{Cr}_{1-x}\text{Ni}_x\text{OsO}_6$ ($x = 0, 0.25, 0.5, 1$) are presented in Fig. 1(a). The patterns for the end compounds ($x = 0$ and 1) indicate that the high-pressure synthesized $\text{Sr}_2\text{CrOsO}_6$ and $\text{Sr}_2\text{NiOsO}_6$ are comparable to those prepared without high pressure by others [9,27]. In addition, the patterns clarify that the Ni substitution results in a systematic peak shift [see Fig. 1(b)], indicating the formation of a solid solution between the end compounds. To the best of our knowledge, the Ni solid solution was produced. Note that an attempt to synthesize the solid solution at $x = 0.75$ was unsuccessful even at 6 GPa; perhaps a much higher-pressure condition is necessary.

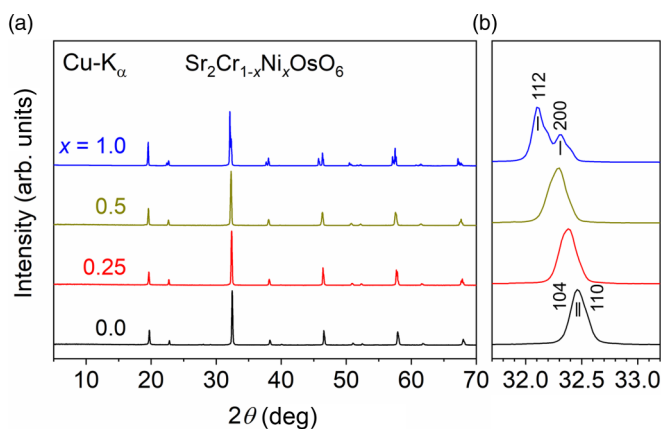


FIG. 1. (a) Powder XRD patterns of $\text{Sr}_2\text{Cr}_{1-x}\text{Ni}_x\text{OsO}_6$ ($x = 0, 0.25, 0.5, 1$) measured at room temperature. (b) Horizontal expansion around the major peaks with hkl indices of 110 and 104 for the trigonal lattice ($R-3$) and 112 and 200 for the tetragonal lattice ($I4/m$).

To investigate the lattice change during the Ni substitution, $\text{Sr}_2\text{Cr}_{1-x}\text{Ni}_x\text{OsO}_6$ powders ($x = 0, 0.25, 0.5, \text{ and } 1$) were studied by synchrotron XRD at temperatures below and above T_C ; room-temperature measurements were conducted for all, and measurements at 750, 550, and 454 K were conducted for, respectively, $\text{Sr}_2\text{CrOsO}_6$ ($x = 0$), $\text{Sr}_2\text{Cr}_{0.75}\text{Ni}_{0.25}\text{OsO}_6$ ($x = 0.25$), and $\text{Sr}_2\text{Cr}_{0.5}\text{Ni}_{0.5}\text{OsO}_6$ ($x = 0.5$). Note that the magnetic transition temperatures were 664(1) K, 519(1) K, 351(1) K, and 37.7(4) K at, respectively, $x = 0, 0.25, 0.5, \text{ and } 1$ (shown later).

The synchrotron XRD patterns for $\text{Sr}_2\text{Cr}_{1-x}\text{Ni}_x\text{OsO}_6$ analyzed by the Rietveld method are presented in Figs. S1 ($x = 0$), S2 ($x = 0.25$), 2 ($x = 0.5$), and S3 ($x = 1$) in the Supplemental Material [28]. To avoid repeatedly displaying similar patterns, the $x = 0.5$ patterns below and above T_C are herein shown as a representative. The crystallographic parameters refined by the analysis are summarized in Tables S1–S7 [28]. Regarding $\text{Sr}_2\text{CrOsO}_6$ ($x = 0$), reasonable agreement between the observation and calculation was attained by employing a cubic model ($Fm-3m$) for the 750 K pattern [Fig. S1(a) and Table S1] and a trigonal model ($R-3$) for the room-temperature pattern [Fig. S1(b) and Table S2] [28]. Note that the same structural transition from cubic to trigonal was observed previously by others [8]. In the analysis, the occupancies at the $3b$ and $3a$ sites (Wyckoff positions) for Os and Cr were refined independently; a small amount of antisite disorder was suggested to have occurred between the $3b$ and $3a$ sites. However, the total chemical sum, $\text{Sr}_2\text{Cr}_{0.96}\text{Os}_{1.04}\text{O}_6$, is very close to the starting composition.

The $\text{Sr}_2\text{Cr}_{0.75}\text{Ni}_{0.25}\text{OsO}_6$ patterns were analyzed in the same manner. Successful refinement was achieved for both patterns at 550 K and room temperature, as shown in Figs. S2(a) and S2(b), respectively [28]. The results suggest that $\text{Sr}_2\text{Cr}_{0.75}\text{Ni}_{0.25}\text{OsO}_6$ crystallizes into a cubic structure ($Fm-3m$) above T_C and transforms to trigonal ($R-3$) below T_C , as does the host compound $\text{Sr}_2\text{CrOsO}_6$.

The synchrotron XRD patterns for $\text{Sr}_2\text{Cr}_{0.5}\text{Ni}_{0.5}\text{OsO}_6$ are presented in Figs. 2(a) and 2(b). The high-temperature structure at 454 K was well refined by the tetragonal model ($I4/m$) rather than the cubic model ($Fm-3m$). In a preliminary analysis, the occupancies at the $2a$ and $2b$ sites for Cr, Ni, and Os were refined without any constraint; the temporal results indicate that the $2a$ site was occupied mostly by Cr and Ni at an approximately 1:1 ratio with a small amount of Os. The $2b$ site was fully occupied by Os. Thus, in the final step, a constraint for the occupancies at the $2a$ site was introduced, as shown in Table S5 [28]. The tetragonal model ($I4/m$) was successful in the analysis of $\text{Sr}_2\text{NiOsO}_6$ (Fig. S3 and Table S7) as well [28]. During this study, the site occupancies for Os and Cr atoms were carefully checked, and a fully ordered Ni and Os arrangement was supported. The result conforms with the previous result for $\text{Sr}_2\text{NiOsO}_6$ obtained by others [27].

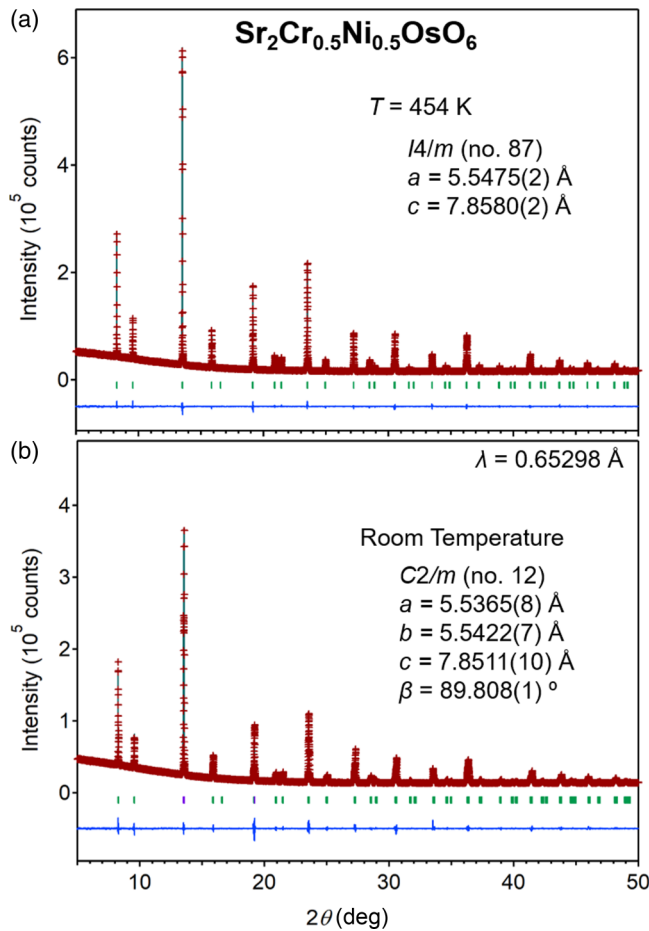


FIG. 2. Rietveld refinement of the powder synchrotron XRD profiles of $\text{Sr}_2\text{Cr}_{0.5}\text{Ni}_{0.5}\text{OsO}_6$ at $\lambda = 0.65298 \text{ \AA}$, collected above and below T_C of 351 K : (a) 454 K and (b) room temperature. The red crosses and green solid lines show the observed and calculated patterns, respectively, with their differences shown at the bottom. The expected Bragg reflections are marked by ticks.

Based on the analysis of $\text{Sr}_2\text{Cr}_{0.5}\text{Ni}_{0.5}\text{OsO}_6$, after being cooled from 454 K to room temperature, a peak split was observed, as shown in Fig. S4 in the Supplemental Material [28]. Therefore, a lower-symmetry model was assumed for the room-temperature structure. Considering the structural models of other double perovskite oxides such as $\text{Sr}_2\text{CoOsO}_6$ [29], $\text{Sr}_2\text{FeIrO}_6$ [30], $\text{Sr}_2\text{FeSbO}_6$ [31], $\text{Sr}_2\text{NiTeO}_6$ [32], and $\text{Sr}_2\text{Ni}_{0.5}\text{Mg}_{0.5}\text{TeO}_6$ [33], we tested the monoclinic ($C2/m$, No. 12) and triclinic ($I-1$, No. 2) models for the room-temperature structure; eventually, a better and reasonable solution was obtained using the monoclinic model ($C2/m$). The refined results are shown in Fig. 2(b) and Table S6 [28].

To further study the slightly distorted room-temperature structure ($C2/m$) of $\text{Sr}_2\text{Cr}_{0.5}\text{Ni}_{0.5}\text{OsO}_6$, the same powder was subjected to an additional examination by electron diffraction; however, the electron diffraction patterns were rather consistent with the tetragonal model ($I4/m$) (Fig. 3). In addition, upon heating and cooling between room temperature and 454 K , the anticipated appearance and disappearance of additional spots was not observed, implying that structural transition did not occur. Besides, Raman spectroscopy

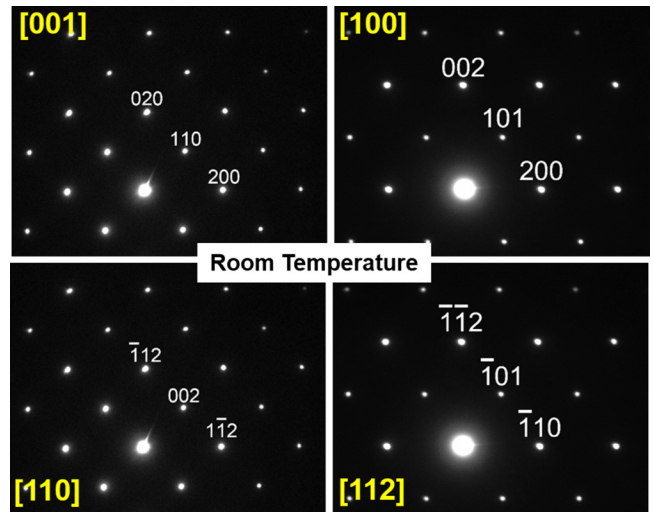


FIG. 3. Electron diffraction patterns for $\text{Sr}_2\text{Cr}_{0.5}\text{Ni}_{0.5}\text{OsO}_6$ observed along four different zone axes at room temperature.

was conducted on the same powder, but the patterns did not support the structural transition in a very clear way (Fig. 4), although features of the magnetic transition ($T_C = 351 \text{ K}$), such as the decrease in intensity by heating, were confirmed. Note that the observed strong and broad peak around 800 cm^{-1} originates from the OsO_6 octahedra [34]. The discrepancies among the sets of data remain to be further investigated.

The crystal structure of the solid solution $\text{Sr}_2\text{Cr}_{1-x}\text{Ni}_x\text{OsO}_6$ ($x = 0, 0.25, 0.5, 1$) shows a symmetry-change from cubic ($Fm-3m$) to tetragonal ($I4/m$) as a function of the Ni concentration, when the temperatures are above their T_C s, as depicted in Fig. 5 (see Table I for details). At room temperature, the crystal structure is trigonal ($R-3$), monoclinic ($C2/m$), or tetragonal ($I4/m$) depending on their Ni concentrations (see Table S8 for details) [28]. These observations suggest that the magnetic transition has a significant impact on the lattice symmetry. Therefore, the cell-volume evolution over the Ni

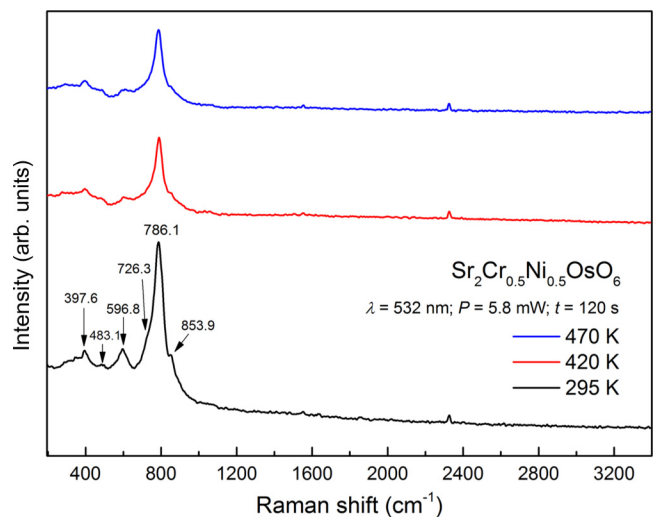


FIG. 4. Raman spectra of $\text{Sr}_2\text{Cr}_{0.5}\text{Ni}_{0.5}\text{OsO}_6$ at 470 , 420 , and 295 K .

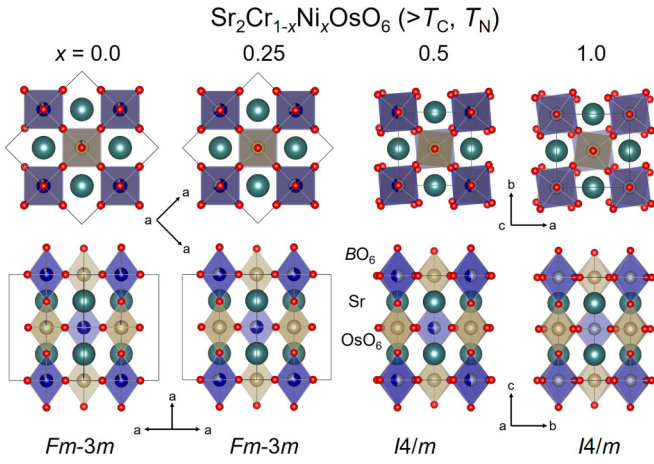


FIG. 5. Structure models for $\text{Sr}_2\text{Cr}_{1-x}\text{Ni}_x\text{OsO}_6$ ($x = 0, 0.25, 0.5, 1.0$). Each is based on the structural data obtained from above T_C : (top) parallel and (bottom) perpendicular to the c axis. Green, blue, gold, and red balls denote Sr, Cr/Ni, Os, and O, respectively.

concentration at room temperature (see Fig. 6) does not show a linear change, probably because the lattice is under the influence of magnetic ordering at different T_C s.

Based on the refined structure parameters of $\text{Sr}_2\text{Cr}_{1-x}\text{Ni}_x\text{OsO}_6$ ($x = 0, 0.25, 0.5, 1$), the bond valence sum (BVS) was calculated and is shown in Tables 1 and

S8 [28]. For Sr, the BVS is close to 2, which is consistent with the divalency over the entire composition range. For Cr and Ni, the BVS at the end compositions indicates trivalency and divalency, respectively. The BVS calculation thus suggests that the electronic configurations at the ends are $\text{Sr}_2\text{Cr}^{3+}\text{Os}^{5+}\text{O}_6$ and $\text{Sr}_2\text{Ni}^{2+}\text{Os}^{6+}\text{O}_6$, as previously reported by others [8,35]. Hence, the valence state of the solid solution may be intermediate between those, but further investigation by methods such as XAS is necessary to discover the true valence state of the solid solution.

B. X-ray absorption spectroscopy (XAS)

The combined soft and hard XAS spectra of the solid-solution $\text{Sr}_2\text{Cr}_{0.5}\text{Ni}_{0.5}\text{OsO}_6$ were measured to investigate the valence state of Ni, Cr, and Os ions. As a start, we first determine the Ni and Cr valence states; Fig. 7(a) shows the Ni- $L_{2,3}$ XAS spectra of $\text{Sr}_2\text{Cr}_{0.5}\text{Ni}_{0.5}\text{OsO}_6$, NiO as a Ni^{2+} reference, and LaNiO_3 as a Ni^{3+} reference (taken from Ref. [36]). The energy position of the Ni- $L_{2,3}$ edge of $\text{Sr}_2\text{Cr}_{0.5}\text{Ni}_{0.5}\text{OsO}_6$ is shifted by more than 1 eV relative to the Ni^{3+} reference, but the multiplet structure and the energy position are identical to those of NiO [37,38]. Thus, the Ni of $\text{Sr}_2\text{Cr}_{0.5}\text{Ni}_{0.5}\text{OsO}_6$ is divalent.

The Cr- $L_{2,3}$ XAS spectra of $\text{Sr}_2\text{Cr}_{0.5}\text{Ni}_{0.5}\text{OsO}_6$, Cr_2O_3 as a Cr^{3+} reference, $\text{Ag}_2\text{Cr}_2\text{O}_7$ as a Cr^{6+} reference, and PbCrO_3 as a mixed-valence reference ($\frac{2}{3}\text{Cr}^{3+} + \frac{1}{3}\text{Cr}^{6+}$, taken from Ref. [39]) are presented in Fig. 7(b). One can see

TABLE I. Lattice and structural parameters at elevated temperatures of $\text{Sr}_2\text{Cr}_{1-x}\text{Ni}_x\text{OsO}_6$ ($x = 0, 0.25, 0.5, 1$) as revealed by synchrotron XRD.

	$x = 0$	$x = 0.25$	$x = 0.5$	$x = 1$
T_C, T_N (K)($=\Theta_W$)	664(1)	519(1)	351(1)	37.7(4)
Sample temp. (K)	750	550	454	R.T.
Space group	$Fm-3m$	$Fm-3m$	$I4/m$	$I4/m$
a (\AA)	7.84460(5)	7.84115(3)	5.5475(2)	5.5320(2)
c (\AA)			7.8580(2)	7.9204(3)
d_{cal} (g/cm^3)	7.149	7.185	7.138	7.127
R_{wp} (%)	1.942	1.785	1.808	2.376
R_p (%)	1.335	1.218	1.222	1.480
R_B (%)	0.831	0.730	0.906	0.908
R_F (%)	0.430	0.348	0.424	0.426
Z	4	4	2	2
$B\text{-O1}$ (\AA) ^a	$1.995(3) \times 6$	$2.0128(16) \times 6$	$2.075(6) \times 2$	$2.060(6) \times 2$
$B\text{-O2}$ (\AA) ^a			$2.046(6) \times 4$	$2.053(5) \times 4$
Os-O1 (\AA) ^b	$1.927(3) \times 6$	$1.9078(16) \times 6$	$1.854(6) \times 2$	$1.900(6) \times 2$
Os-O2 (\AA) ^b			$1.890(6) \times 4$	$1.899(5) \times 4$
$B\text{-O1-Os}$ (deg)	180.0	180.0	180.0	180.0
$B\text{-O2-Os}$ (deg)			170.4(4)	163.5(3)
Average (deg)	180.0	180.0	175.2(4)	171.8(3)
		BVS ^c		
Sr	2.04	2.04	2.04	2.18
Cr/Ni	2.89 (Cr)			2.03 (Ni)
Os	5.11	5.39/5.94	5.39/5.94	6.07

^a B is a transition metal at $4b$ in the cubic structure and $2a$ in the tetragonal structure.

^bOs is at $4a$ in the cubic structure and $2b$ in the tetragonal structure.

^cBVS = $\sum_{i=1}^N v_i$, where $v_i = e^{(R_0 - l_i)/b_0}$, N is the coordination number, l is the bond length, $b_0 = 0.37$ [67], $R_0(\text{Sr}^{2+}) = 2.118$ [67], $R_0(\text{Cr}^{3+}) = 1.724$ [67], $R_0(\text{Ni}^{2+}) = 1.654$ [67], $R_0(\text{Os}^{5+}) = 1.868$ [68,69], and $R_0(\text{Os}^{6+}) = 1.904$ with $b_0(\text{Os}^{6+}) = 0.375$ [70]. The BVS before the slash was calculated with $R_0(\text{Os}^{5+})$, while that after the slash was calculated with $R_0(\text{Os}^{6+})$.

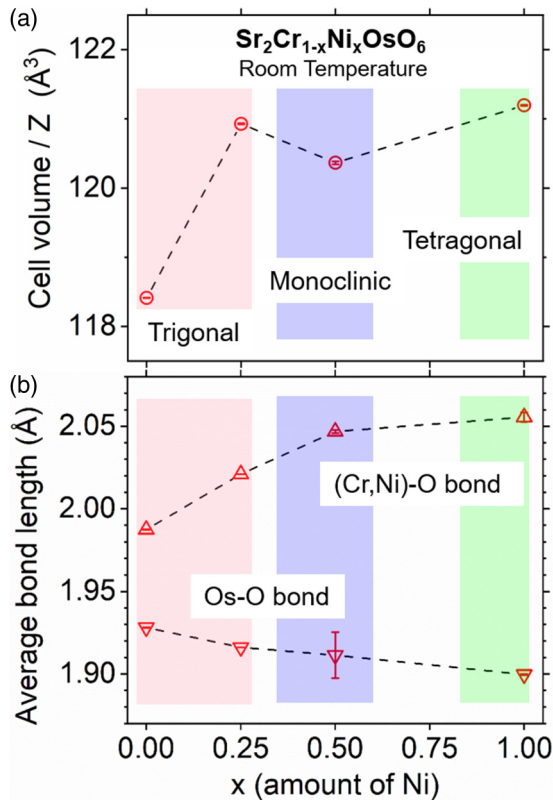


FIG. 6. (a) Variations of the cell volume/ Z and (b) the average bond lengths in the B -site octahedra of $\text{Sr}_2\text{Cr}_{1-x}\text{Ni}_x\text{OsO}_6$ ($x = 0, 0.25, 0.5, 1.0$), measured by synchrotron XRD at room temperature; $Z = 3, 2$, and 2 for the $R-3$, $C2/m$, and $I4/m$ models, respectively.

with increase of the Cr valence state from bottom to top, the $\text{Cr-}L_{2,3}$ spectrum shifts to the higher energy, indicating its high sensitivity to the Cr valence state. The main peak at 580.8 eV in the $\text{Ag}_2\text{Cr}_2\text{O}_7$ spectrum is characteristic of the $3d^0$ initial state of Cr^{6+} [40,41] and it shifts by 3.1 eV to the higher energy relative to the main peak of the Cr_2O_3 spectrum. The multiplet spectral feature of the $\text{Cr-}L_{2,3}$ edge of $\text{Sr}_2\text{Cr}_{0.5}\text{Ni}_{0.5}\text{OsO}_6$ is very similar to that of the mixed-valence PbCrO_3 with an average Cr^{4+} state, demonstrating the similar Cr valence state of $\text{Sr}_2\text{Cr}_{0.5}\text{Ni}_{0.5}\text{OsO}_6$. The coexistence of Cr^{3+} and Cr^{6+} at a ratio of 2:1 in $\text{Sr}_2\text{Cr}_{0.5}\text{Ni}_{0.5}\text{OsO}_6$ is supported by XMCD measurements (discussed later). Reminiscently of the synchrotron XRD study of $\text{Sr}_2\text{Cr}_{0.5}\text{Ni}_{0.5}\text{OsO}_6$, the high-temperature structure ($I4/m$) transforms into a lower-symmetry structure ($C2/m$) by cooling. The complex electronic configuration of Cr may be associated with the lowering mechanism.

Having determined the Cr^{4+} average state and Ni^{2+} state of $\text{Sr}_2\text{Cr}_{0.5}\text{Ni}_{0.5}\text{OsO}_6$, we have further confirmed the Os^{5+} state as expected by the charge balance. In Fig. 7(c), the $\text{Os-}L_3$ edge of $\text{Sr}_2\text{Cr}_{0.5}\text{Ni}_{0.5}\text{OsO}_6$ is presented together with those of $\text{La}_2\text{MgOsO}_6$ as an Os^{4+} reference [42], $\text{Sr}_2\text{FeOsO}_6$ as an Os^{5+} reference [43], and $\text{Ba}_2\text{NiOsO}_6$ as an Os^{6+} reference [44]. The energy position of the $\text{Os-}L_3$ edge of $\text{Sr}_2\text{Cr}_{0.5}\text{Ni}_{0.5}\text{OsO}_6$ locates between those of the Os^{4+} reference ($\text{La}_2\text{MgOsO}_6$) and the Os^{6+} reference ($\text{Ba}_2\text{NiOsO}_6$). In addition, it is at the same position of the

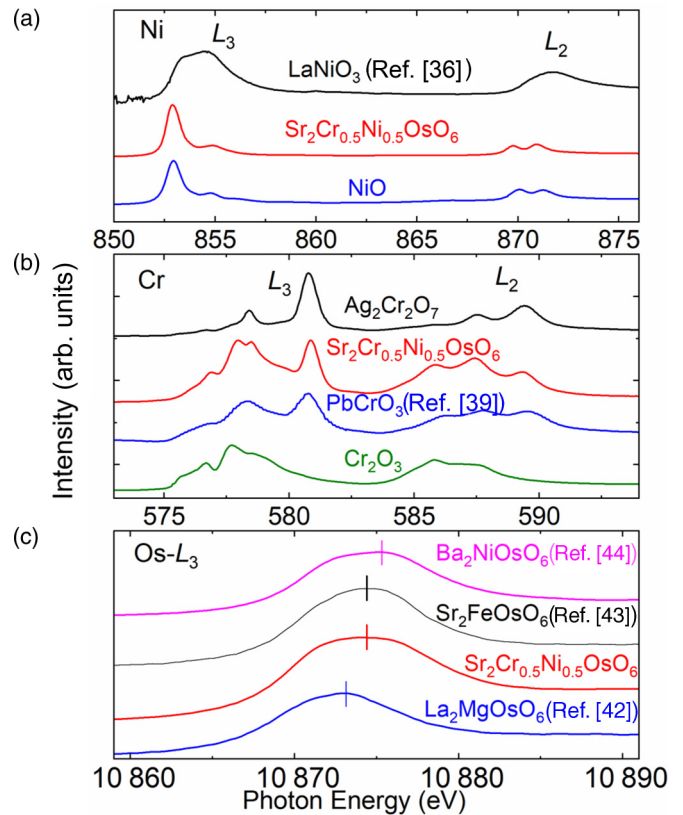


FIG. 7. (a) The $\text{Ni-}L_{2,3}$ XAS spectra of $\text{Sr}_2\text{Cr}_{0.5}\text{Ni}_{0.5}\text{OsO}_6$ together with NiO and LaNiO_3 (from Ref. [36]) as references. (b) The $\text{Cr-}L_{2,3}$ XAS spectra of $\text{Sr}_2\text{Cr}_{0.5}\text{Ni}_{0.5}\text{OsO}_6$ together with Cr_2O_3 , PbCrO_3 (from Ref. [39]), $\text{Ag}_2\text{Cr}_2\text{O}_7$ as references. (c) The $\text{Os-}L_3$ XAS spectra of $\text{Sr}_2\text{Cr}_{0.5}\text{Ni}_{0.5}\text{OsO}_6$ with $\text{La}_2\text{MgOsO}_6$ (from Ref. [42]), $\text{Sr}_2\text{FeOsO}_6$ (from Ref. [43]) and $\text{Ba}_2\text{NiOsO}_6$ (from Ref. [44]) as references.

Os^{5+} reference ($\text{Sr}_2\text{FeOsO}_6$), indicating the same valence state of Os^{5+} fulfilling the charge balance requirement. Thus, we can rewrite the composition of $\text{Sr}_2\text{Cr}_{0.5}\text{Ni}_{0.5}\text{OsO}_6$ as $\text{Sr}_2(\text{Cr}^{3+}_{2/3}\text{Cr}^{6+}_{1/3})_{0.5}\text{Ni}^{2+}_{0.5}\text{Os}^{5+}\text{O}_6$.

C. Electrical and magnetic properties

The temperature dependence of the electrical resistivity (ρ) of $\text{Sr}_2\text{Cr}_{1-x}\text{Ni}_x\text{OsO}_6$ ($x = 0, 0.25, 0.5, 1$) is shown in Fig. 8. The ρ of all compounds continuously increases upon cooling, indicating semiconductivity. The Arrhenius law was applied to the data for each at high temperatures (>200 K) to estimate their activation energy (E_a). The analytical formula was $\rho = \rho_0 \exp(E_a/k_B T)$, where ρ_0 and k_B , respectively, are a temperature-independent constant and the Boltzmann constant. The data fitting for $\text{Sr}_2\text{Cr}_{0.5}\text{Ni}_{0.5}\text{OsO}_6$ is displayed as an example by a solid line. Consequently, the increase in E_a with the Ni substitution was confirmed (inset of Fig. 8). The activation energy deduced from Arrhenius law at the high temperatures is related to the band gap energy ($\approx 2E_a$) as the intrinsic resistivity is provided by the thermal activation of charge carriers over the band gap [45,46]. The increase of E_a implies the band gap may be tunable through Ni substitution since Ni has different electron configuration from Cr. The

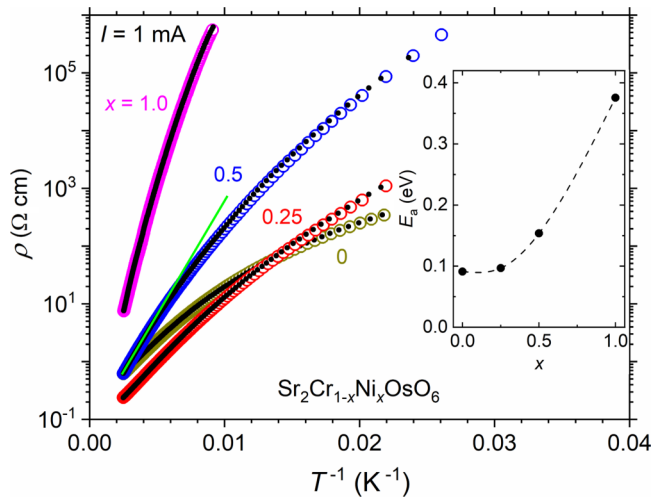


FIG. 8. (a) The temperature dependence of electrical resistivity of polycrystalline $\text{Sr}_2\text{Cr}_{1-x}\text{Ni}_x\text{OsO}_6$ ($x = 0, 0.25, 0.5, 1$) upon cooling (solid dot) and heating (open circles). Inset is a variation of the activation energy, E_a , over x , estimated by the plots. The dashed curve is a guide to the eye.

mechanism of the tunable band gap requires further band-structure calculation.

In Fig. 8, nonlinear behavior at low temperatures suggests that variable-range-hopping conduction probably originates from the localized centers [47,48]. For comparison, the $T^{-1/2}$ and $T^{-1/4}$ scales are given in Fig. S5 in the Supplemental Material [28]; clarifying that an expected linear behavior occurs on the $T^{-1/2}$ scale rather than the $T^{-1/4}$ scale. The characteristic temperature dependence suggests that the Efros-Shklovskii model is better for describing the hopping conduction of $\text{Sr}_2\text{Cr}_{0.5}\text{Ni}_{0.5}\text{OsO}_6$ than the Mott model [47,48]. A soft gap in the density of states near the Fermi level may have been created by Coulomb interaction [48]. The other $\text{Sr}_2\text{CrOsO}_6$ and $\text{Sr}_2\text{Cr}_{0.75}\text{Ni}_{0.25}\text{OsO}_6$ show similar hopping behaviors below ~ 100 K, but $\text{Sr}_2\text{NiOsO}_6$ does not [see Figs. S6(a) and 6(b)] [28].

Below 100 K, an additional transport measurement was conducted for $\text{Sr}_2\text{Cr}_{0.5}\text{Ni}_{0.5}\text{OsO}_6$ as an example using an impedance analyzer. The temperature dependence of the real part of the dielectric constant (ϵ') and dielectric loss ($\tan\delta$) is shown in Figs. 9(a) and 9(b), respectively. High dielectric constant values at temperatures higher than ~ 60 K are typical of the Maxwell-Wagner effect associated with the electrode and grain-boundary polarization due to the presence of mobile charge carriers. As the temperature decreases and the charge carriers freeze out, ϵ' drops and becomes frequency independent and reaches approximately 30 (< 20 K), which is a typical value for many complex perovskites (i.e., 20–40). Because of the carrier freezing, the contribution to ϵ' can only arise from the optical phonons.

Consistently with the $\epsilon'-T$ behavior, the dielectric loss below ~ 10 K is small and is frequency independent because of the carriers freezing [Fig. 9(b)]. With increasing temperature, $\tan\delta$ increases and becomes frequency dependent. An increase in the dielectric loss can be explained by the onset of charge carrier hopping. Interestingly, the $\tan\delta$ value shows

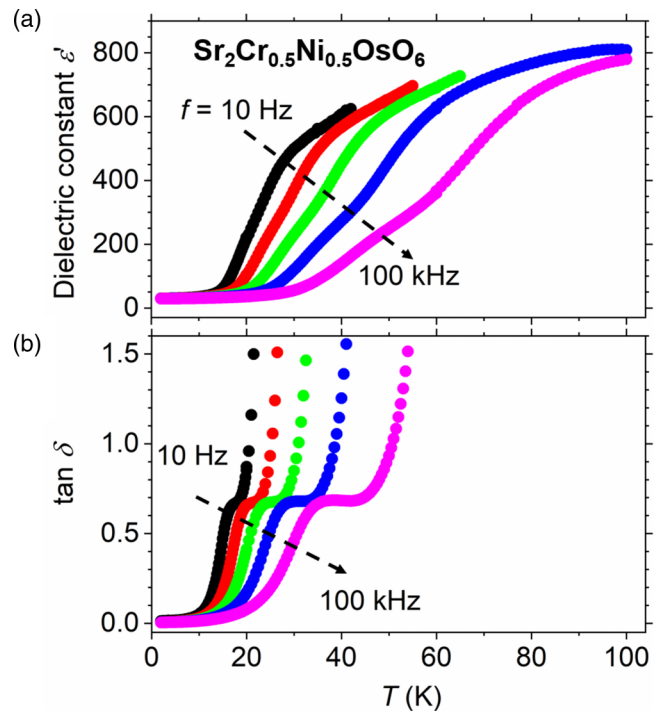


FIG. 9. (a) Temperature dependence of the dielectric constant and (b) dielectric loss of $\text{Sr}_2\text{Cr}_{0.5}\text{Ni}_{0.5}\text{OsO}_6$ at frequencies of $f = 1 \times 10^1, 10^2, 10^3, 10^4$, and 10^5 Hz.

a plateau before increasing again at higher temperatures. The plateau may be attributed to the acoustic-phonon-assisted (localized) hopping of the charge carriers bound to point defects. With a further increase in temperature, $\tan\delta$ sharply increases, indicating that the charge carriers become increasingly conductive.

Nyquist plots of the complex impedance of $\text{Sr}_2\text{Cr}_{0.5}\text{Ni}_{0.5}\text{OsO}_6$ are shown in Fig. S7 [28]. In the temperature range of 30–60 K, a single arc ($Z''-Z'$) grows by cooling. At the lowest frequency (i.e., 10 Hz), the arc intercepts the Z' axis at an impedance value consistent with the dc resistivity. This indicates that the grain boundary and sample-electrode interface resistances are negligible. With further cooling, the charge carriers freeze out at temperatures below 30 K and the arc no longer intercepts the Z' axis because the specific resistivity becomes very high ($> 2 \times 10^7 \Omega \text{ cm}$).

The temperature dependence of C_p for these compounds is plotted in Fig. 10. The low-temperature part is replotted to the C_p/T vs T^2 form (inset of Fig. 10). An approximated Debye model $C_p/T = \gamma + \beta_0 T$ [2], in which γ and β_0 are, respectively, the Sommerfeld coefficient and a constant, was applied to fit the low-temperature part. The analysis yielded γ values of $3.9(2) \times 10^{-3} \text{ J mol}^{-1} \text{ K}^{-2}$ and β_0 of $5.50(4) \times 10^{-4} \text{ J mol}^{-1} \text{ K}^{-4}$ for $\text{Sr}_2\text{Cr}_{0.5}\text{Ni}_{0.5}\text{OsO}_6$. The small γ may be associated with the variable-range-hopping conduction. The Debye temperature was calculated from β_0 to be 327.9(8) K. The parameters for the other compounds are listed in Table II, indicating a weak composition dependence. Note that the parameters of $\text{Sr}_2\text{NiOsO}_6$ could not be deduced in the same manner because of the poor linearity. The origin of the unusual C_p of $\text{Sr}_2\text{NiOsO}_6$ is left for future study.

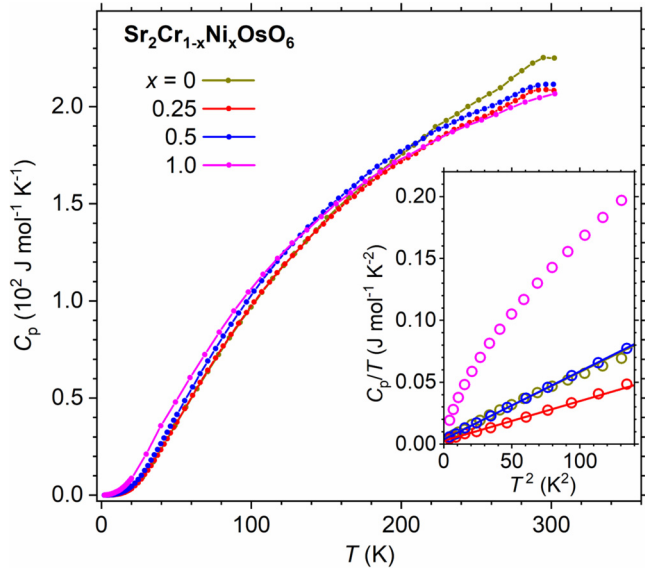


FIG. 10. Temperature dependence of the specific heat for $\text{Sr}_2\text{Cr}_{1-x}\text{Ni}_x\text{OsO}_6$ ($x = 0, 0.25, 0.5, 1$). The upper axis corresponds to the Dulong-Petit limit of the lattice-specific heat. (Inset) Linear fit (solid lines) to the C_p/T vs T^2 curves for the low-temperature region.

The temperature dependence of χ in an applied magnetic field of 10 kOe is shown in Fig. 11(a). In each plot for $\text{Sr}_2\text{Cr}_{1-x}\text{Ni}_x\text{OsO}_6$ (except $x = 1$), two independent sets of the data were combined because the T_C was too high to be measured on a single instrument. $\text{Sr}_2\text{NiOsO}_6$ shows a sharp peak in the ZFC and FC curves at 38 K; this is indicative of antiferromagnetic (AFM) ordering. The magnetic behavior is comparable to that observed by others for $\text{Sr}_2\text{NiOsO}_6$ synthesized without high pressure [27]. In contrast, the χ vs T curves for each $\text{Sr}_2\text{Cr}_{1-x}\text{Ni}_x\text{OsO}_6$ ($x = 0, 0.25, 0.5$) show pop-ups at 664(1) K, 519(1) K, and 351(1) K, respectively, suggesting the occurrence of long-range ferromagnetic (FM) or FIM ordering.

In the χ - T curves for $\text{Sr}_2\text{CrOsO}_6$, nonmonotonic temperature dependence below T_C was confirmed, as previously observed by others [8,9]. It was argued that the different temperature dependencies of the Os and Cr magnetic sublattices may account for the nonmonotonic behavior [9]. In contrast, the χ - T plots for $\text{Sr}_2\text{Cr}_{0.5}\text{Ni}_{0.5}\text{OsO}_6$ and $\text{Sr}_2\text{Cr}_{0.75}\text{Ni}_{0.25}\text{OsO}_6$ are rather monotonic (see the FC curves).

It has been argued that a $3d^3$ - $5d^3$ hybrid oxide such as $\text{Sr}_2\text{CrOsO}_6$ shows a relatively high T_C as does a d^3 oxide

[49–51]. Indeed, when $\text{Os}^{5+}(5d^3)$ of $\text{Sr}_2\text{CrOsO}_6$ is replaced by $\text{Re}^{5+}(5d^2)$ or $\text{W}^{5+}(5d^1)$, the magnetic transition temperature (725 K [8]) decreases to 635 K ($\text{Sr}_2\text{CrReO}_6$ [3]) or 458 K (Sr_2CrWO_6 [6]). Therefore, it is not unexpected that the substitution of Ni^{2+} for Cr^{3+} results in a decreasing T_C . The Ni concentration dependence of the magnetic transition temperature (T_C and T_N) is summarized in the inset of Fig. 11(a), which indeed shows a linear feature.

The $1/\chi$ vs T plot of these compounds displays a linear behavior above T_C (T_N), as shown in Fig. 11(b). However, the high-temperature-end part does not follow the linear trend because of the measurement accuracy (see the fluctuation of the data points). Thus, the end part was not considered in this analysis. $\text{Sr}_2\text{Cr}_{0.5}\text{Ni}_{0.5}\text{OsO}_6$ exhibits linear behavior in the temperature range 390–470 K; therefore, the Curie-Weiss law $1/\chi = (T - \Theta_W)/C$ was applied to the range, giving the C (the Curie constant) of 0.292(1) and Θ_W (Weiss temperature) of 351(1) K. The effective magnetic moment (μ_{eff}) was deduced from C : $\mu_{\text{eff}} = 1.53(1)\mu_B$, although the theoretical spin-only moment of $\text{Sr}_2(\text{Cr}^{3+}_{2/3}\text{Cr}^{6+}_{1/3})_{0.5}\text{Ni}^{2+}_{0.5}\text{Os}^{5+}\text{O}_6$ is $4.90\mu_B$ [calculated from $\text{Cr}^{3+}(3d^3)$, $\text{Cr}^{6+}(3d^0)$, $\text{Ni}^{2+}(3d^8)$, and $\text{Os}^{5+}(5d^3)$]. The theoretical value is too large to account for this observation. Perhaps an impact from the SOC on the electronic state needs to be considered. The analysis was also applied to the plots for the other compounds, from which the Curie-Weiss parameters were deduced, as shown in Table II. It appears that the μ_{eff} of $\text{Sr}_2\text{Cr}_{0.5}\text{Ni}_{0.5}\text{OsO}_6$ is intermediate between the experimental μ_{eff} of $\text{Sr}_2\text{CrOsO}_6$ [$0.831(3)\mu_B$] and $\text{Sr}_2\text{NiOsO}_6$ [$3.29(1)\mu_B$]. The linear trend can also be seen for the Weiss temperature, which declines with increasing Ni concentrations [see the inset of Fig. 11(a)]. In contrast, $\text{Sr}_2\text{Cr}_{0.75}\text{Ni}_{0.25}\text{OsO}_6$ shows a second magnetic anomaly at ~ 540 K, which is an indication of the occurrence of an additional magnetic transition or the presence of a magnetic impurity. To figure it out, further measurement and study are required; for example, neutron diffraction and electron microscopy may help [52].

The isothermal magnetization of $\text{Sr}_2\text{Cr}_{1-x}\text{Ni}_x\text{OsO}_6$ ($x = 0, 0.25, 0.5, 1$) at 5 K is shown in Fig. 12. Nonlinear behavior is evident in the plots for $\text{Sr}_2\text{Cr}_{0.5}\text{Ni}_{0.5}\text{OsO}_6$ as well as the other Cr-rich compounds $\text{Sr}_2\text{Cr}_{1-x}\text{Ni}_x\text{OsO}_6$ ($x = 0$ and 0.25). It shows that the saturation magnetization (M_{sat}) is enhanced by the half Ni substitution more than 6 times that of $\text{Sr}_2\text{CrOsO}_6$ [9]; the M_{sat} of $\text{Sr}_2\text{Cr}_{0.5}\text{Ni}_{0.5}\text{OsO}_6$ is $\sim 1.2\mu_B/\text{f.u.}$. The enhancement is preserved even when the temperature was elevated to room temperature [see Fig. 11(a)].

TABLE II. Sommerfeld coefficient (γ), constant β_0 , Debye temperature, and Curie-Weiss parameters of $\text{Sr}_2\text{Cr}_{1-x}\text{Ni}_x\text{OsO}_6$ ($x = 0, 0.25, 0.5, 1$).

$\text{Sr}_2\text{Cr}_{1-x}\text{Ni}_x\text{OsO}_6$	$x = 0$	$x = 0.25$	$x = 0.5$	$x = 1$
γ ($10^{-3} \text{ J mol}^{-1} \text{ K}^{-2}$)	4.3(4)	2.8(3)	3.9(2)	–
β_0 ($10^{-4} \text{ J mol}^{-1} \text{ K}^{-4}$)	5.39(9)	3.21(5)	5.50(4)	–
Debye temperature (K)	330(2)	392(2)	328(1)	–
C ($\text{emu mol}^{-1} \text{ Oe}^{-1} \text{ K}$)	0.0863(7)	0.165(1)	0.292(1)	1.35(1)
μ_{eff} ($\mu_B/\text{f.u.}$)	0.831(3)	1.15(1)	1.53(1)	3.29(1)
Θ_W (K)	+664(1)	+519(1)	+351(1)	+37.7(4)

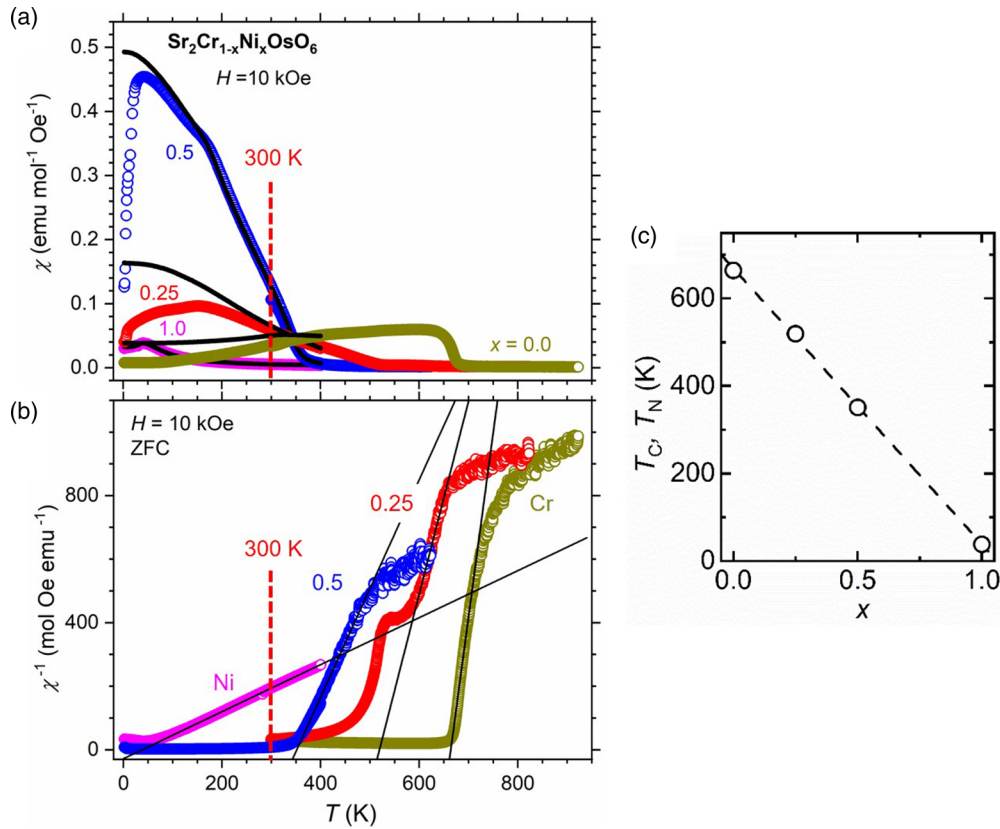


FIG. 11. (a) Temperature dependence of ZFC (open dot) and FC (solid dot) susceptibilities ($H = 10 \text{ kOe}$) for $\text{Sr}_2\text{Cr}_{1-x}\text{Ni}_x\text{OsO}_6$ ($x = 0, 0.25, 0.5, 1$). (b) Alternative plots of the same data. The solid line indicates fitting to a linear part of each curve. (c) Weiss temperatures over x .

D. X-ray magnetic circular dichroism (XMCD)

In order to further understand the magnetic properties of $\text{Sr}_2\text{Cr}_{0.5}\text{Ni}_{0.5}\text{OsO}_6$, we performed XMCD measurements at the Cr- $L_{2,3}$, Ni- $L_{2,3}$, and Os- $L_{2,3}$ edges. XMCD is an element-specific method that can determine the magnetic orientations of the various ions and also what their spin and orbital

contributions to the magnetic moments are. As shown in Fig. 13, both the Ni and Os XMCD possess the same negative (positive) sign at the L_3 (L_2) edge, which is indicative of FM coupling between Ni and Os. However, the Cr XMCD shows a positive (negative) sign at the L_3 (L_2) edge, just opposite to Os and Ni. Hence, Cr is antiferromagnetically coupled with the Os and also the Ni in $\text{Sr}_2\text{Cr}_{0.5}\text{Ni}_{0.5}\text{OsO}_6$. The spin and orbital moments obtained from the sum rule calculations are listed in Table III.

The spin (m_{spin}) and orbital (m_{orb}) contributions of $\text{Ni}^{2+}(3d^8)$ were evaluated, respectively, to be $1.39 \mu_B/\text{Ni}^{2+}$ and $0.39 \mu_B/\text{Ni}^{2+}$. The magnitude of the spin moment is smaller than the theoretical value of $\text{Ni}^{2+}(3d^8)$, while the orbital contribution is large (the ratio $m_{\text{orb}}/m_{\text{spin}}$ is 0.28). Such a sizable orbital moment of Ni^{2+} was also observed for other Ni oxides. This is due to the fact that the SOC introduces an orbital component via a mixing of the e_g and t_{2g} orbitals because the $d-d$ multiplet interaction is larger than the effective crystal-field splitting [53–55].

In case of the element Cr, the spin sum rule calculation cannot be applied because of the significant overlap between the L_3 and L_2 edges [26,56]. To obtain a correct spin moment from the experimental Cr- $L_{2,3}$ XMCD spectra, we performed full-atomic-multiplet ligand-field calculations using the XTLS 9.0 code [57]. The parameters used are listed in Ref. [58]. The calculated Cr XMCD spectra with $\text{Cr}^{3+} : \text{Cr}^{6+} = 2 : 1$ are displayed in Fig. 14(b), which readily reproduces the experiment [Fig. 14(a)]. The Cr^{3+} XMCD and Cr^{6+} XAS spectra are

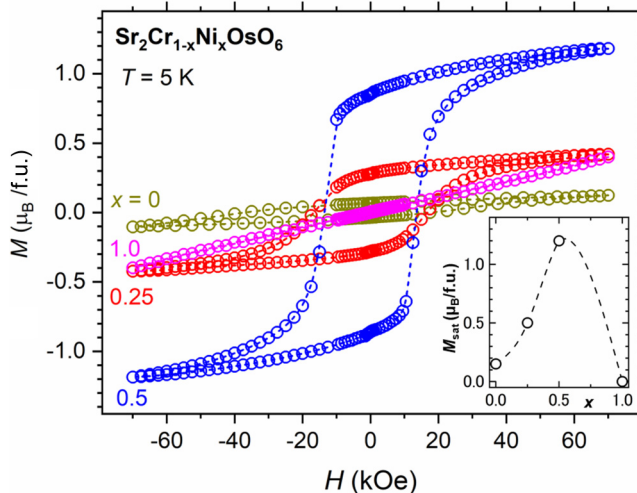


FIG. 12. Isothermal magnetization curves at 5 K for $\text{Sr}_2\text{Cr}_{1-x}\text{Ni}_x\text{OsO}_6$ ($x = 0, 0.25, 0.5, 1$). Inset: the saturation magnetization estimated from the curves.

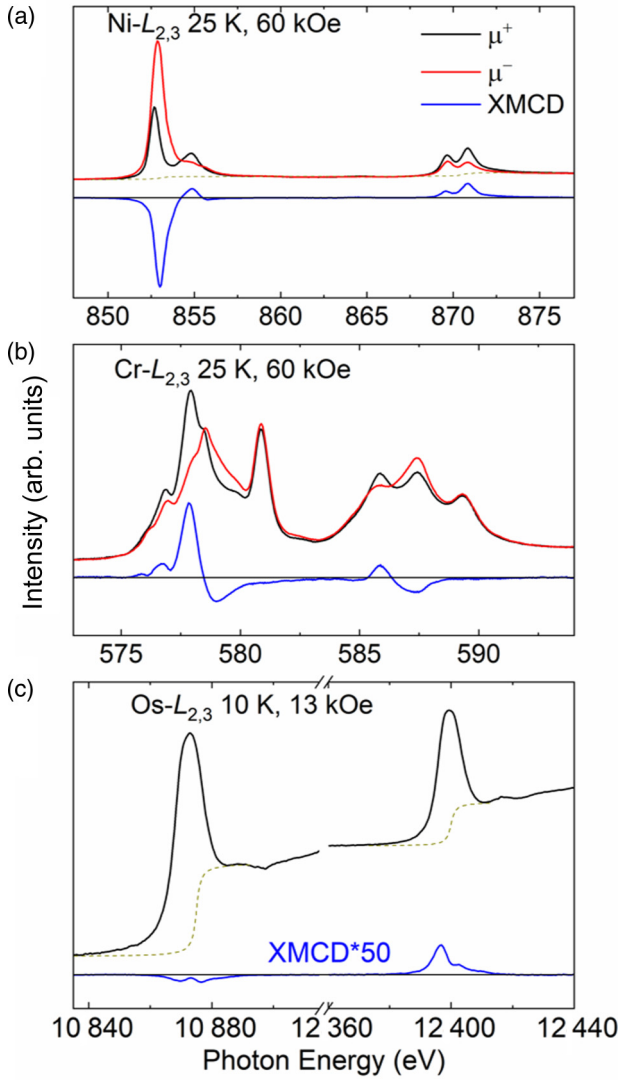


FIG. 13. (a) Ni- $L_{2,3}$, (b) Cr- $L_{2,3}$, and (c) Os- $L_{2,3}$ XMCD spectra of $\text{Sr}_2\text{Cr}_{0.5}\text{Ni}_{0.5}\text{OsO}_6$.

also shown in Figs. 14(c) and 14(d), respectively. The calculated spin and orbital moments of Cr^{3+} are listed in Table III. It should be noted that the magnetic contribution of Cr comes only from the Cr^{3+} in the compound ($\text{Cr} = \frac{2}{3}\text{Cr}^{3+} + \frac{1}{3}\text{Cr}^{6+}$);

TABLE III. Spin (m_{spin}) and orbital (m_{orb}) moments of $\text{Sr}_2\text{Cr}_{0.5}\text{Ni}_{0.5}\text{OsO}_6$ deduced by XMCD.

Atom	Ni	Cr^{3+}	Os
$m_{\text{spin}} (\mu_{\text{B}}/\text{atom})$	1.39	-1.84	-
$m_{\text{orb}} (\mu_{\text{B}}/\text{atom})$	0.39	0.041	-
$m_{\text{spin}} + m_{\text{orb}} (\mu_{\text{B}}/\text{atom})$	1.78	-1.80	-
$m_{\text{spin}} + m_{\text{orb}} (\mu_{\text{B}}/\text{f.u.})^{\text{a}}$	0.89	-0.60	(0.91) ^b
$m_{\text{orbit}}/m_{\text{spin}}$	0.28	-0.022	-0.16

^aThe unit conversion is based on the experimental formula $\text{Sr}_2(\text{Cr}^{3+}_{2/3}\text{Cr}^{6+}_{1/3})_{0.5}\text{Ni}^{2+}_{0.5}\text{Os}^{5+}\text{O}_6$.

^bEstimated from the isothermal magnetization ($M_{\text{sat}} \sim 1.2 \mu_{\text{B}}/\text{f.u.}$) at 5 K.

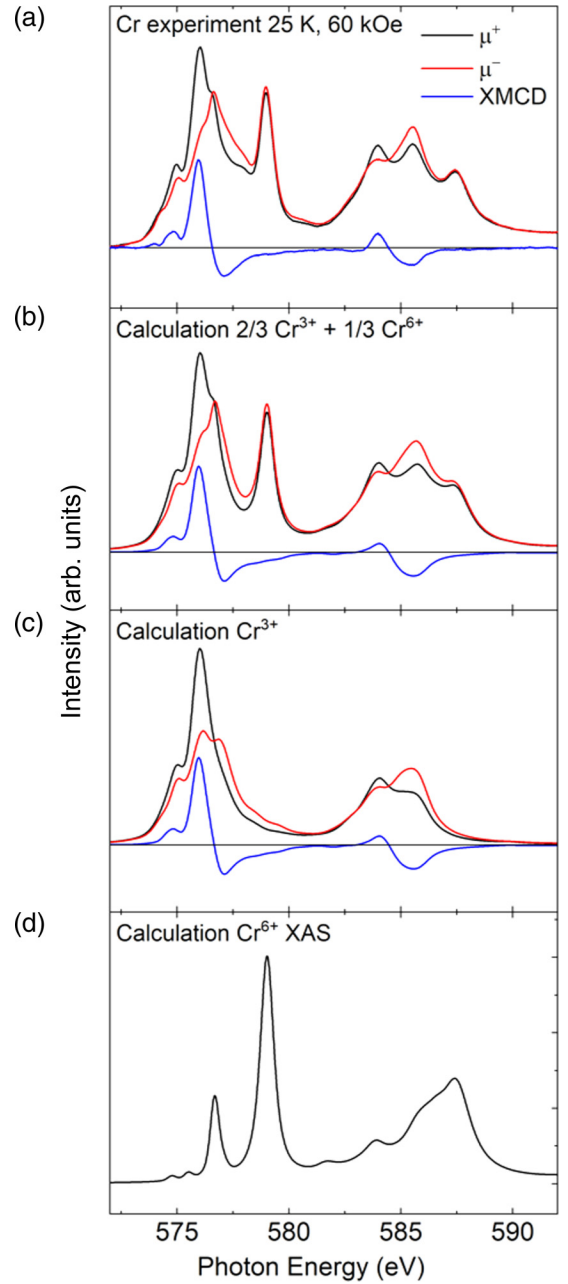


FIG. 14. (a) Experimental and (b) calculated Cr XMCD spectra of $\text{Sr}_2\text{Cr}_{0.5}\text{Ni}_{0.5}\text{OsO}_6$. (c) Calculated Cr^{3+} XMCD spectra. (d) Calculated Cr^{6+} XAS spectra.

therefore, it is reasonable to use a factor of $\frac{1}{3}$ ($=0.5 \times \frac{2}{3}$) in the unit conversion in Table III (from μ_{B}/Cr to $\mu_{\text{B}}/\text{f.u.}$).

The absolute value of the magnetic moment on Os^{5+} obtained from the sum rule is less accurate than the ratio $m_{\text{orb}}/m_{\text{spin}}$ due to a low external magnetic field of 13 kOe, where the Os^{5+} was not magnetically saturated. The ratio $m_{\text{orb}}/m_{\text{spin}}$ is -0.16 for Os^{5+} , which is very close to the values obtained from other Os^{5+} compounds [42,59].

The magnetic moments for Cr, Ni of $\text{Sr}_2\text{Cr}_{0.5}\text{Ni}_{0.5}\text{OsO}_6$ are tabulated in Table III. Although the net magnetic moment of Os^{5+} was not obtained from the XMCD data, the value can be estimated from the difference between M_{sat}

($\approx 1.2 \mu_B/\text{f.u.}$) and the magnetic moments of $3d$ ions (Ni^{2+} and Cr^{3+}), which gives a value of $0.91 \mu_B/\text{f.u.}$ for Os^{5+} of $\text{Sr}_2\text{Cr}_{0.5}\text{Ni}_{0.5}\text{OsO}_6$. This value is close to the value of Os^{5+} ($0.82 \mu_B$) obtained by neutron diffraction reported by others for $\text{Sr}_2\text{CrOsO}_6$ at 5 K [9]. The moment of Os^{5+} of both $\text{Sr}_2\text{CrOsO}_6$ and $\text{Sr}_2\text{Cr}_{0.5}\text{Ni}_{0.5}\text{OsO}_6$ is smaller than the values observed for the other Os^{5+} perovskites [60–62]; the reason has remained elusive [9].

IV. DISCUSSION

The high- T_C FIM properties of $\text{Sr}_2\text{CrOsO}_6$ have been studied by many experiments and theoretical calculations over the past two decades, but the mechanism of the remarkably high T_C with a small M_{sat} remains an open question. In this study, the high-pressure synthesized $\text{Sr}_2\text{CrOsO}_6$ displayed a T_C (664 K) and magnetization ($0.124 \mu_B/\text{f.u.}$ at 70 kOe) comparable with the values reported previously by others [9]. In addition, a Ni substitution series $\text{Sr}_2\text{Cr}_{1-x}\text{Ni}_x\text{OsO}_6$ ($x = 0.25, 0.5$) was synthesized under high-pressure and high-temperature conditions. It appears that the Ni substitution results in a reduced T_C (from 664 to 351 K), but the M_{sat} was unexpectedly enhanced by more than a factor of 6. The enhancement is preserved even at room temperature.

In the ferrimagnetic $\text{Sr}_2\text{CrOsO}_6$ compound, the Cr and Os moments are antiparallel aligned in spin. With the moments almost equal in size, the resulting net magnetization becomes rather small. In $\text{Sr}_2\text{Cr}_{0.5}\text{Ni}_{0.5}\text{OsO}_6$, we find from our XMCD measurements that the Os ions are still antiferromagnetically coupled to the Cr. Excitingly, we observe that the Ni moments are ferromagnetically aligned to the Os. The replacement of antiferromagnetic Cr by ferromagnetic Ni therefore explains naturally the swift increase of the net magnetism in this Ni-substituted system.

$\text{Sr}_2\text{Cr}_{0.5}\text{Ni}_{0.5}\text{OsO}_6$ is a complex system because three transition metals coexist at the perovskite B site. The oxidation states of Cr, Ni, and Os found in the XAS experiment indicate that $\text{Sr}_2\text{Cr}_{0.5}\text{Ni}_{0.5}\text{OsO}_6$ and $\text{Sr}_2\text{CrOsO}_6$ partly share the same electronic $3d^3$ - $5d^3$ configuration for the nearest-neighbor Cr^{3+} - O - Os^{5+} bonds in the lattice. $\text{Sr}_2\text{Cr}_{0.5}\text{Ni}_{0.5}\text{OsO}_6$ is a magnetic insulator; therefore, its properties can be characterized by the magnetic superexchange interactions running among $\text{Cr}^{3+}(3d^3)$, $\text{Ni}^{2+}(3d^8)$, and $\text{Os}^{5+}(5d^3)$. The Cr^{3+} - Os^{5+} , Cr^{3+} - Ni^{2+} , and Ni^{2+} - Os^{5+} interactions are expected to be AFM, FM, and FM, respectively, according to the Goodenough-Kanamori rule [63,64].

We infer that the strong antiferromagnetic exchange interaction of the $3d^3$ - $5d^3$ configuration associated with the Cr^{3+} - O - Os^{5+} bond still accounts for the robust high- T_C ferrimagnetism of the Ni-substituted series. We find from the XMCD experiments that the Ni and Os are spin parallel, consistent with the expectation that the exchange interaction of the $3d^8$ - $5d^3$ configuration of the Ni^{2+} - O - Os^{5+} bond is ferromagnetic. We would like to note, however, that SrLaNiOsO_6 is an antiferromagnet while BaLaNiOsO_6 shows ferromagnetic correlations [65], so bond angles or structural details in general are important in determining the strength of the Ni^{2+} - O - Os^{5+} ferromagnetic exchange interactions relative to other exchange interactions present in the crystal

[65]. In our case, this Ni^{2+} - O - Os^{5+} ferromagnetic exchange interaction is apparently stronger than that of the also ferromagnetic Ni^{2+} - O - Cr^{3+} since the Cr is spin antiparallel with the Ni and Os as revealed by our XMCD measurements. A similar situation was revealed for other $3d$ - $5d$ oxides such as $\text{RCu}_3\text{Fe}_2\text{Os}_2\text{O}_{12}$ [43,66], in which the strong Cu-O-Os interaction forces the spins of Cu^{2+} and Fe^{3+} to be parallel with each other. These results suggest that the larger $5d$ orbital of the Os allows for a stronger virtual hopping from the Ni than the smaller $3d$ orbital of the Cr.

Finally, we must note that the presence of the ferromagnetic Ni^{2+} - O - Os^{5+} interactions constitutes a competition with the antiferromagnetic Cr^{3+} - O - Os^{5+} interactions that are responsible in the first place for the FIM order in $\text{Sr}_2\text{CrOsO}_6$. Therefore upon Ni for Cr substitution, this together also with the lower number of Cr^{3+} - O - Os^{5+} bonds will weaken the FIM order of $\text{Sr}_2\text{CrOsO}_6$, resulting in lowering the T_C from 664 K ($\text{Sr}_2\text{CrOsO}_6$) to 351 K ($\text{Sr}_2\text{Cr}_{0.5}\text{Ni}_{0.5}\text{OsO}_6$).

V. CONCLUSION

With T_C beyond room temperature, the complex $3d^3$ - $5d^3$ double perovskite insulator $\text{Sr}_2\text{Cr}_{0.5}\text{Ni}_{0.5}\text{OsO}_6$ has more than sixfold the improved high- T_C FIM properties of the $3d^3$ - $5d^3$ insulator $\text{Sr}_2\text{CrOsO}_6$, M_{sat} . The XAS measurements reveal that the valence state of $\text{Os}^{5+}(5d^3)$ does not change via Ni^{2+} substitution, but instead, the nonmagnetic $\text{Cr}^{6+}(3d^0)$ is partly generated among coexisting $\text{Cr}^{3+}(3d^3)$. Therefore, the $3d^3$ - $5d^3$ configuration of the Cr^{3+} - O - Os^{5+} bonds are still firmly present in the lattice; this accounts for the robust high- T_C FIM properties of the Ni-substituted series. Moreover, we found from the XMCD experiment that the Ni and Os are ferromagnetically coupled; this explains the large increase of the magnetization since spin-parallel Ni ions are replacing spin-antiparallel Cr ions in the ferrimagnetic Os-Cr perovskite.

ACKNOWLEDGMENTS

We thank Shalika Ram Bhandari and Madhav Prasad Ghimire for the discussions on this topic. The synchrotron radiation experiments were performed at the NIMS synchrotron X-ray station at SPring-8 with the approval of the Japan Synchrotron Radiation Research Institute (Proposals No. 2019B4500, No. 2019A4501, and No. 2018B4502), at the XMCD endstation of BOREAS beamline at ALBA Synchrotron Light Source (Proposal No. 2018082933), and at the dispersive XAS endstation of ODE beamline at Synchrotron SOLEIL. This study was supported in part by JSPS KAKENHI Grants No. JP20H05276 and No. 19H05819, a research grant from Nippon Sheet Glass Foundation for Materials Science and Engineering (#Grant No. 40-37), and Innovative Science and Technology Initiative for Security (Grant No. JPJ004596), ATLA, Japan. The research in Dresden was partially supported by the Deutsche Forschungsgemeinschaft through SFB 1143 (Project-Id 247310070).

The manuscript was written through contributions from all authors. All authors have given their approval for the final version of the manuscript.

The authors declare no competing financial interests.

- [1] K.-I. Kobayashi, T. Kimura, H. Sawada, K. Terakura, and Y. Tokura, *Nature* **395**, 677 (1998).
- [2] J. M. De Teresa, D. Serrate, C. Ritter, J. Blasco, M. R. Ibarra, L. Morellon, and W. Tokarz, *Phys. Rev. B* **71**, 092408 (2005).
- [3] H. Kato, T. Okuda, Y. Okimoto, Y. Tomioka, Y. Takenoya, A. Ohkubo, M. Kawasaki, and Y. Tokura, *Appl. Phys. Lett.* **81**, 328 (2002).
- [4] Y. Moritomo, S. Xu, A. Machida, T. Akimoto, E. Nishibori, M. Takata, and M. Sakata, *Phys. Rev. B* **61**, R7827(R) (2000).
- [5] K.-I. Kobayashi, T. Kimura, Y. Tomioka, H. Sawada, K. Terakura, and Y. Tokura, *Phys. Rev. B* **59**, 11159 (1999).
- [6] J. B. Philipp, P. Majewski, L. Alff, A. Erb, R. Gross, T. Graf, M. S. Brandt, J. Simon, T. Walther, W. Mader, D. Topwal, and D. D. Sarma, *Phys. Rev. B* **68**, 144431 (2003).
- [7] T. K. Mandal, C. Felser, M. Greenblatt, and J. Kübler, *Phys. Rev. B* **78**, 134431 (2008).
- [8] Y. Krockenberger, K. Mogare, M. Reehuis, M. Tovar, M. Jansen, G. Vaitheeswaran, V. Kanchana, F. Bultmark, A. Delin, F. Wilhelm, A. Rogalev, A. Winkler, and L. Alff, *Phys. Rev. B* **75**, 020404(R) (2007).
- [9] R. Morrow, J. R. Soliz, A. J. Hauser, J. C. Gallagher, M. A. Susner, M. D. Sumption, A. A. Aczel, J. Yan, F. Yang, and P. M. Woodward, *J. Solid State Chem.* **238**, 46 (2016).
- [10] K.-W. Lee and W. E. Pickett, *Phys. Rev. B* **77**, 115101 (2008).
- [11] O. N. Meetei, O. Erten, M. Randeria, N. Trivedi, and P. Woodward, *Phys. Rev. Lett.* **110**, 087203 (2013).
- [12] P. Majewski, S. Geprägs, A. Boger, M. Opel, A. Erb, R. Gross, G. Vaitheeswaran, V. Kanchana, A. Delin, F. Wilhelm, A. Rogalev, and L. Alff, *Phys. Rev. B* **72**, 132402 (2005).
- [13] P. Majewski, S. Geprägs, O. Sanganas, M. Opel, R. Gross, F. Wilhelm, A. Rogalev, and L. Alff, *Appl. Phys. Lett.* **87**, 202503 (2005).
- [14] M. Wojcik, E. Jedryka, S. Nadolski, D. Rubi, C. Frontera, J. Fontcuberta, B. Jurca, N. Drago, and P. Berthet, *Phys. Rev. B* **71**, 104410 (2005).
- [15] J. Navarro, C. Frontera, L. Balcells, B. Martinez, and J. Fontcuberta, *Phys. Rev. B* **64**, 092411 (2001).
- [16] S. Geprägs, P. Majewski, R. Gross, C. Ritter, and L. Alff, *J. Appl. Phys.* **99**, 08J102 (2006).
- [17] Y. K. Wakabayashi, Y. Krockenberger, N. Tsujimoto, T. Boykin, S. Tsuneyuki, Y. Taniyasu, and H. Yamamoto, *Nat. Commun.* **10**, 1 (2019).
- [18] M. Tanaka, Y. Katsuya, Y. Matsushita, and O. Sakata, *J. Ceram. Soc. Jpn.* **121**, 287 (2013).
- [19] M. Tanaka, Y. Katsuya, and A. Yamamoto, *Rev. Sci. Instrum.* **79**, 075106 (2008).
- [20] K. Momma and F. Izumi, *J. Appl. Crystallogr.* **44**, 1272 (2011).
- [21] F. Izumi and T. Ikeda, *Mater. Sci. Forum* **321–324**, 198 (2000).
- [22] A. Barla, J. Nicolás, D. Cocco, S. M. Valvidares, J. Herrero-Martín, P. Gargiani, J. Moldes, C. Ruget, E. Pellegrin, and S. Ferrer, *J. Synchrotron Radiat.* **23**, 1507 (2016).
- [23] B. T. Thole, P. Carra, F. Sette, and G. van der Laan, *Phys. Rev. Lett.* **68**, 1943 (1992).
- [24] P. Carra, B. T. Thole, M. Altarelli, and X. Wang, *Phys. Rev. Lett.* **70**, 694 (1993).
- [25] J. Stöhr and H. König, *Phys. Rev. Lett.* **75**, 3748 (1995).
- [26] Y. Teramura, A. Tanaka, and T. Jo, *J. Phys. Soc. Jpn.* **65**, 1053 (1996).
- [27] R. Macquart, S.-J. Kim, W. R. Gemmill, J. K. Stalick, Y. Lee, T. Vogt, and H.-C. zur Loye, *Inorg. Chem.* **44**, 9676 (2005).
- [28] See Supplemental Material at <http://link.aps.org/supplemental/10.1103/PhysRevB.102.184418> for tables showing the crystallographic parameters of $\text{Sr}_2\text{Cr}_{1-x}\text{Ni}_x\text{OsO}_6$ ($x = 0, 0.25, 0.5, 1$), Rietveld refinement of the powder synchrotron XRD profiles of $\text{Sr}_2\text{Cr}_{1-x}\text{Ni}_x\text{OsO}_6$ ($x = 0, 0.25, 1$), an expanded view of the synchrotron XRD pattern for $\text{Sr}_2\text{Cr}_{0.5}\text{Ni}_{0.5}\text{OsO}_6$, and alternative resistivity plots and complex impedance plots of $\text{Sr}_2\text{Cr}_{0.5}\text{Ni}_{0.5}\text{OsO}_6$.
- [29] A. Kumar Paul, M. Reehuis, C. Felser, P. M. Abdala, and M. Jansen, *Z. Anorg. Allg. Chem.* **639**, 2421 (2013).
- [30] I. Qasim, P. E. R. Blanchard, S. Liu, C. Tang, B. J. Kennedy, M. Avdeev, and J. A. Kimpton, *J. Solid State Chem.* **206**, 242 (2013).
- [31] A. Faik, J. M. Igartua, E. Iturbe-Zabalzo, and G. J. Cuello, *J. Mol. Struct.* **963**, 145 (2010).
- [32] L. O.-S. Martín, J. P. Chapman, G. Cuello, J. González-Calbet, M. I. Arriortua, and T. Rojo, *Z. Anorg. Allg. Chem.* **631**, 2127 (2005).
- [33] B. Orayech, L. Ortega-San-Martin, I. Urcelay-Olabarria, L. Lezama, T. Rojo, M. I. Arriortua, and J. M. Igartua, *Dalton Trans.* **45**, 14378 (2016).
- [34] R. Sereika, K. Yamaura, Y. Jia, S. Zhang, C. Jin, H. Yoon, M. Y. Jeong, M. J. Han, D. L. Brewes, S. M. Heald, S. Sinogeikin, Y. Ding, and H.-K. Mao, *Mater. Today Phys.* **8**, 18 (2019).
- [35] C. Tian, A. C. Wibowo, H.-C. zur Loye, and M.-H. Whangbo, *Inorg. Chem.* **50**, 4142 (2011).
- [36] H. Guo, Z. W. Li, L. Zhao, Z. Hu, C. F. Chang, C.-Y. Kuo, W. Schmidt, A. Piovano, T. W. Pi, O. Sobolev, D. I. Khomskii, L. H. Tjeng, and A. C. Komarek, *Nat. Commun.* **9**, 43 (2018).
- [37] D. Alders, J. Vogei, C. Levelut, S. D. Peacor, T. Hibma, M. Sacchi, L. H. Tjeng, C. T. Chen, G. Van der Laan, and B. T. Thole, *EPL* **32**, 259 (1995).
- [38] M. W. Haverkort, S. I. Csiszar, Z. Hu, S. Altieri, A. Tanaka, H. H. Hsieh, H.-J. Lin, C. T. Chen, T. Hibma, and L. H. Tjeng, *Phys. Rev. B* **69**, 020408(R) (2004).
- [39] M. Wu, L. Zheng, S. Chu, Z. Qin, X.-J. Chen, C. Lin, Z. Tang, and T. Hu, *J. Phys. Chem. C* **118**, 23274 (2014).
- [40] F. M. F. de Groot, J. C. Fuggle, B. T. Thole, and G. A. Sawatzky, *Phys. Rev. B* **41**, 928 (1990).
- [41] J. Schlappa, C. F. Chang, Z. Hu, E. Schierle, H. Ott, E. Weschke, G. Kaindl, M. Huijben, G. Rijnders, D. H. A. Blank, L. H. Tjeng, and C. Schüßler-Langeheine, *J. Phys.: Condens. Matter.* **24**, 035501 (2012).
- [42] Q. Zhao, M. Liu, J. Dai, H. Deng, Y. Yin, L. Zhou, J. Yang, Z. Hu, S. Agrestini, K. Chen, E. Pellegrin, M. Valvidares, L. Nataf, F. Baudelet, L. H. Tjeng, Y.-F. Yang, C. Jin, and Y. Long, *Inorg. Chem.* **55**, 9816 (2016).
- [43] H. Deng, M. Liu, J. Dai, Z. Hu, C. Kuo, Y. Yin, J. Yang, X. Wang, Q. Zhao, Y. Xu, Z. Fu, J. Cai, H. Guo, K. Jin, T. Pi, Y. Soo, G. Zhou, J. Cheng, K. Chen, P. Ohresser, Y.-F. Yang, C. Jin, L.-H. Tjeng, and Y. Long, *Phys. Rev. B* **94**, 024414 (2016).
- [44] H. L. Feng, S. Calder, M. P. Ghimire, Y.-H. Yuan, Y. Shirako, Y. Tsujimoto, Y. Matsushita, Z. Hu, C.-Y. Kuo, L. H. Tjeng, T.-W. Pi, Y.-L. Soo, J. He, M. Tanaka, Y. Katsuya, M. Richter, and K. Yamaura, *Phys. Rev. B* **94**, 235158 (2016).
- [45] C. Michel, S. D. Baranovskii, P. J. Klar, P. Thomas, and B. Goldlücke, *Appl. Phys. Lett.* **89**, 112116 (2006).
- [46] J. Ye, T. Baldauf, S. Mattauch, N. Paul, and A. Paul, *Commun. Phys.* **2**, 114 (2019).

- [47] A. J. E. Rettie, H. C. Lee, L. G. Marshall, J.-F. Lin, C. Capan, J. Lindemuth, J. S. McCloy, J. Zhou, A. J. Bard, and C. B. Mullins, *J. Am. Chem. Soc.* **135**, 11389 (2013).
- [48] A. L. Efros and B. I. Shklovskii, *J. Phys. C: Solid State Phys.* **8**, L49 (1975).
- [49] W. Tian, C. Svoboda, M. Ochi, M. Matsuda, H. B. Cao, J.-G. Cheng, B. C. Sales, D. G. Mandrus, R. Arita, N. Trivedi, and J.-Q. Yan, *Phys. Rev. B* **92**, 100404(R) (2015).
- [50] S. Calder, V. O. Garlea, D. F. McMorrow, M. D. Lumsden, M. B. Stone, J. C. Lang, J.-W. Kim, J. A. Schlueter, Y. G. Shi, K. Yamaura, Y. S. Sun, Y. Tsujimoto, and A. D. Christianson, *Phys. Rev. Lett.* **108**, 257209 (2012).
- [51] E. E. Rodriguez, F. Poineau, A. Llobet, B. J. Kennedy, M. Avdeev, G. J. Thorogood, M. L. Carter, R. Seshadri, D. J. Singh, and A. K. Cheetham, *Phys. Rev. Lett.* **106**, 067201 (2011).
- [52] H. Gabold, Z. Luan, N. Paul, M. Opel, P. Müller-Buschbaum, M. Law, and A. Paul, *Sci. Rep.* **8**, 1 (2018).
- [53] K. K. Wolff, S. Agrestini, A. Tanaka, M. Jansen, and L. H. Tjeng, *Z. Anorg. Allg. Chem.* **643**, 2095 (2017).
- [54] V. Fernandez, C. Vettier, F. de Bergevin, C. Giles, and W. Neubeck, *Phys. Rev. B* **57**, 7870 (1998).
- [55] R. J. Radwanski and Z. Ropka, *Phys. B (Amsterdam, Neth.)* **345**, 107 (2004).
- [56] C. Piamonteze, P. Miedema, and F. M. F. de Groot, *Phys. Rev. B* **80**, 184410 (2009).
- [57] A. Tanaka and T. Jo, *J. Phys. Soc. Jpn.* **63**, 2788 (1994).
- [58] Parameters used in cluster calculations (eV). For Cr^{3+} ion: $U_{dd} = 5.5$, $U_{cd} = 7.0$, $\Delta = 5.5$, $10Dq = 0.8$, $V(t_{2g}) = 1.56$, $V(e_g) = 2.94$; Slater integrals were set to 75% of Hartree-Fock values. For Cr^{6+} ion: $U_{dd} = 5.5$, $U_{cd} = 7.0$, $\Delta = 0$, $10Dq = 0.3$, $V(t_{2g}) = 2.05$, $V(e_g) = 3.86$; Slater integrals were set to 75% of Hartree-Fock values.
- [59] Y. H. Matsuda, J. L. Her, S. Michimura, T. Inami, M. Suzuki, N. Kawamura, M. Mizumaki, K. Kindo, J. Yamamura, and Z. Hiroi, *Phys. Rev. B* **84**, 174431 (2011).
- [60] A. E. Taylor, R. Morrow, D. J. Singh, S. Calder, M. D. Lumsden, P. M. Woodward, and A. D. Christianson, *Phys. Rev. B* **91**, 100406(R) (2015).
- [61] L. S. I. Veiga, G. Fabbris, M. van Veenendaal, N. M. Souza-Neto, H. L. Feng, K. Yamaura, and D. Haskel, *Phys. Rev. B* **91**, 235135 (2015).
- [62] A. K. Paul, A. Sarapulova, P. Adler, M. Reehuis, S. Kanungo, D. Mikhailova, W. Schnelle, Z. Hu, C. Kuo, V. Siruguri, S. Rayaprol, Y. Soo, B. Yan, C. Felser, L. H. Tjeng, and M. Jansen, *Z. Anorg. Allg. Chem.* **641**, 197 (2015).
- [63] J. B. Goodenough, *Phys. Rev.* **100**, 564 (1955).
- [64] J. Kanamori, *J. Phys. Chem. Solids* **10**, 87 (1959).
- [65] H. L. Feng, W. Schnelle, L. H. Tjeng, and M. Jansen, *Solid State Commun.* **243**, 49 (2016).
- [66] X. Wang, M. Liu, X. Shen, Z. Liu, Z. Hu, K. Chen, P. Ohresser, L. Nataf, F. O. Baudelet, H.-J. Lin, C.-T. Chen, Y.-L. Soo, Y.-F. Yang, C. Jin, and Y. Long, *Inorg. Chem.* **58**, 320 (2019).
- [67] N. E. Brese and M. O'keeffe, *Acta Crystallogr., Sect. B: Struct. Sci., Cryst. Eng. Mater.* **47**, 192 (1991).
- [68] D. Altermatt and I. D. Brown, *Acta Crystallogr., Sect. B: Struct. Sci., Cryst. Eng. Mater.* **41**, 240 (1985).
- [69] I. D. Brown and D. Altermatt, *Acta Crystallogr., Sect. B: Struct. Sci., Cryst. Eng. Mater.* **41**, 244 (1985).
- [70] J.-I. Yamaura, S. Yonezawa, Y. Muraoka, and Z. Hiroi, *J. Solid State Chem.* **179**, 336 (2006).